

A Polydopamine-Coated Strategy of Mn-Based Prussian Blue Cathode Enabled Mn Dissolution Suppression for Aqueous Zinc Ion Batteries

Hao Ouyang, Hankun Zhang, Kexuan Wang, Lei Luo, Heng Li,* Jilei Liu, and Shi Chen*

The manganese hexacyanoferrate (MnHCF) is a promising cathode material in aqueous zinc-ion batteries (AZIBs). However, MnHCF suffers from low structural stability due to abundant $[\text{Fe}(\text{CN})_4]^{2-}$ vacancies and manganese dissolution. Herein, ethylenediaminetetraacetic acid (EDTA) is used as a chelating agent to regulate the precipitation process, and low-defect polyhedral MnHCF particles are obtained. To suppress manganese dissolution, polydopamine (PDA) conductive polymer is coated on MnHCF (PDA@MnHCF) as a protection layer. The PDA layer successfully slows down manganese (Mn) dissolution and even gradually raises the capacity during the first 100 cycles. Through

dQ/dV fitting, the rise in capacity can be understood as the increased contribution of ZnHCF and MnO_2 , which partially compensated for the decrease in MnHCF contribution. As a result, PDA@MnHCF exhibits superior electrochemical performance with a high specific capacity of 100.7 mAh g^{-1} at 0.2 A g^{-1} , while bare MnHCF fails at the 190th cycle with 63.6 mAh g^{-1} . PDA@MnHCF can also maintain more than twice the specific capacity (45.5 mAh g^{-1}) than bare MnHCF (22.6 mAh g^{-1}) at 2.0 A g^{-1} after 2000 cycles. The results not only found a feasible method to suppress the dissolution of Mn but also quantitatively revealed how electrochemical evolution of MnHCF occurs in AZIBs.

1. Introduction

Aqueous zinc ion battery (AZIB) is one of the most promising candidates for large-scale energy storage due to the intrinsic safety from its nonflammable aqueous electrolytes. Moreover, the Zn metal anode used in AZIBs has various advantages, such as high theoretical capacity (820 mAh g^{-1}), low redox potential (-0.762 V vs. standard hydrogen electrode potential), and low cost, making

AZIBs competitive among various batteries under research.^[1–7] As a promising cathode material, Prussian blue analogues (PBAs) have a robust 3D framework composed of cyanide groups and coordinated metal ions, providing sufficient space for cation insertion. The metal ions act as the active sites participating in redox reactions on the cathode side.^[8] The PBAs also have several advantages, like low cost, nontoxicity, simple synthesis conditions, and environmental friendliness.^[9,10] The chemical formula of PBAs can be written as $\text{AM}_1[\text{M}_2(\text{CN})_6]$. The A site is usually occupied by alkaline metals, like Li, Na, and K. The M₁ site is occupied by transition metals such as Mn, Fe, Co, Ni, Zn, etc., while M₂ site is occupied by Fe.

Among various PBAs materials, manganese hexacyanoferrate (MnHCF) has been considered a competitive cathode candidate in AZIBs due to abundance of manganese element and high discharge voltage of 1.6 V .^[11–18] However, the MnHCF suffers from the dissolution of manganese ions, which results in poor cycling performance. During the charging process, Mn^{2+} is oxidized to Mn^{3+} . But the Mn^{3+} is susceptible to the disproportionation reactions and generates Mn^{2+} and Mn^{4+} due to the Jahn-Teller effect. Moreover, the disproportionation reactions lead to lattice distortion, leading to structural collapse. In the case of potassium manganese(II) hexacyanoferrate,^[19,20] the structural deformation caused by the Jahn-Teller effect results in a transformation of the crystal structure from a cubic phase ($\text{KMn(II)[Fe(III)(CN)}_6\text{]}$) to a tetragonal phase ($\text{Mn(III)[Fe(III)(CN)}_6\text{]}$).^[21,22] The strain generated by this deformation destabilizes the crystal lattice, leading to a gradual dissolution of Mn ions. Therefore, the disproportionation of Mn^{3+} ions and dissolution of Mn^{2+} ions are believed to be responsible for the cyclic instability of many manganese-containing compounds.^[19–21,23–26] In the meantime, Zn^{2+} in the electrolyte could replace the original Mn sites, resulting in the

H. Ouyang, H. Zhang, K. Wang, L. Luo, S. Chen
Institute of Applied Physics and Materials Engineering
University of Macau
Macao, SAR 999078, P. R. China
E-mail: shichen@um.edu.mo

H. Li
State Key Laboratory of High-Performance Ceramics and Superfine Microstructure
Shanghai Institute of Ceramics
Chinese Academy of Sciences
Shanghai 200050, P. R. China
E-mail: liheng@mail.sic.ac.cn

J. Liu
College of Materials Science and Engineering
Hunan Joint International Laboratory of Advanced Materials and Technology of Clean Energy
Hunan Province Key Laboratory for Advanced Carbon Materials and Applied Technology
Hunan University
Changsha, Hunan 410082, P. R. China

 Supporting information for this article is available on the WWW under <https://doi.org/10.1002/batt.202500247>

 © 2025 The Author(s). *Batteries & Supercaps* published by Wiley-VCH GmbH. This is an open access article under the terms of the Creative Commons Attribution-NonCommercial License, which permits use, distribution and reproduction in any medium, provided the original work is properly cited and is not used for commercial purposes.

generation of the zinc(II) hexacyanoferrate (ZnHCF).^[27,28] Owing to the electrochemically inertness of Zn²⁺ in ZnHCF, the specific capacity of the cathode decreases further during cycling process.^[29,30] Therefore, the suppression of manganese dissolution in MnHCF is essential to improving the cycling stability of MnHCF.

Currently, many strategies including elemental doping, structural modulation, and surface coating have been reported to improve the capacity and cycling stability of PBAs.^[31–33] Among these methods, coating is a promising method as it can effectively separate Mn ions in contact with water molecules and thus suppress its dissolution. However, the mechanism on how MnHCF degradation suppression is not fully understood. Conductive polymers are promising candidate for coating layer due to its dual benefits on conductivity improvement and flexibility, which could withstand structural deformation generated during Zn ion insertion/extraction.^[26,32] Among various conductive polymers, dopamine (DA) has attracted a lot of attentions due to its unique self-polymerization and high adhesion properties. It can be oxidized and self-polymerized into polydopamine (PDA) owing to its abundant functional groups such as catechol and amine groups (Figure S1, Supporting Information), which can be easily adhered to or coated on various material surfaces. Moreover, it is compatible with the aqueous electrolyte as a hydrophilic material. PDA has recently been investigated for use as a coating layer on electrode surfaces. A report that coating the PDA around a zinc metal anode significantly enhanced interfacial contact in an aqueous solution, achieving fast desolvation of Zn²⁺ ion, thus lowering the energy barrier for Zn²⁺ ions migration and increasing the diffusion rate.^[34,35] Therefore,

polymerization of DA onto MnHCF surfaces is considered a promising strategy for retarding manganese dissolution. In addition, the flexible PDA layer can accommodate lattice strain during the ion insertion and extraction processes.^[36–40]

In this work, we prepared high-crystalline polyhedral MnHCF particles using ethylenediaminetetraacetic acid (EDTA) as chelating agent to slow down the precipitation reaction rate. The polyhedral MnHCF particles were coated by PDA layer using in situ polymerization (PDA@MnHCF). With PDA coating, the dissolution of manganese was significantly reduced. For the quantitative dQ/dV analysis at the 50th cycle, the PDA@MnHCF maintains 23.8% of capacity contribution from manganese ions while the bare MnHCF show nearly zero contribution. In the meantime, the PDA coating could retain the dissolved manganese ions in the form of MnO₂, which temporarily contributes 10% of total capacity at 1.34 V, inducing a capacity rise within the first 100 cycles.^[16] As a result, the PDA@MnHCF exhibits superior electrochemical performances with a high specific capacity of 100.7 mAh g⁻¹ at 0.2 A g⁻¹ and excellent cycling stability with no capacity decay over 2000 cycles at 2.0 A g⁻¹. While MnHCF battery failed at 190 cycles with the capacity of 64.6 mAh g⁻¹ at 0.2 A g⁻¹.

2. Result and Discussion

The morphologies of the synthesized MnHCF without EDTA, with EDTA, and further coated with PDA were characterized by SEM. As shown in Figure 1a, without EDTA, the MnHCF showed irregular morphology as well as significant agglomeration due to quick

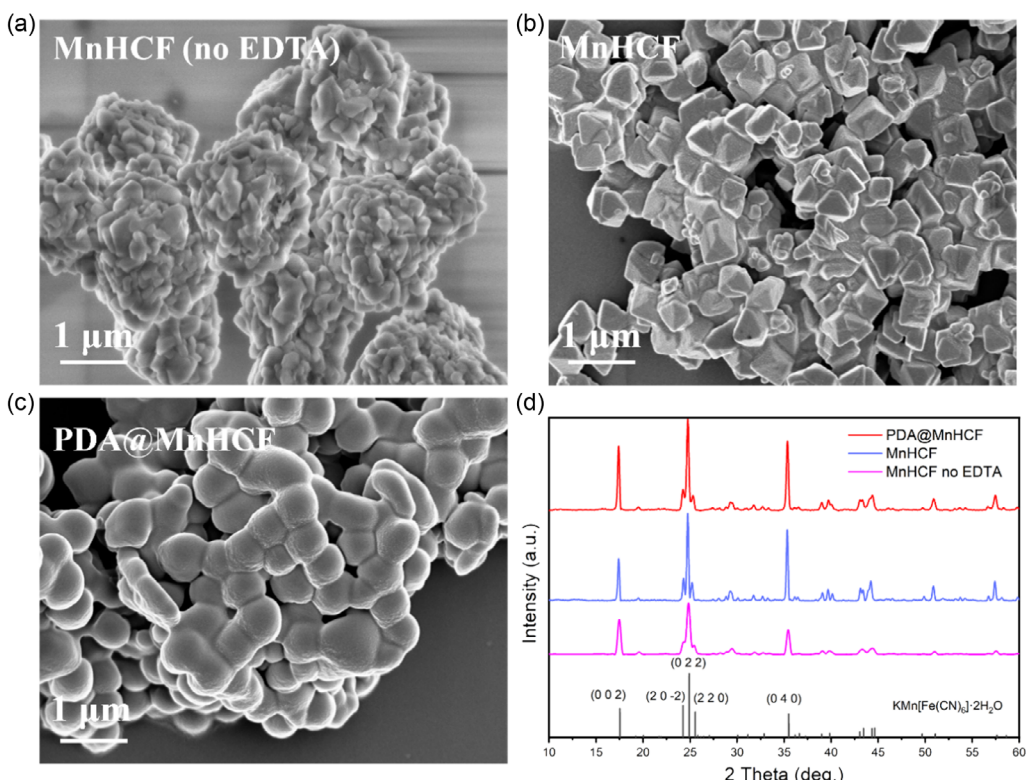


Figure 1. The SEM images of a) MnHCF (no EDTA), b) MnHCF, and c) PDA@MnHCF. d) The XRD patterns of MnHCF (no EDTA), MnHCF, and PDA@MnHCF.

precipitation. With EDTA, the MnHCF sample exhibits smaller crystal size with polyhedral morphology, which can be attributed to slower crystallization process from the chelation effect of EDTA to reduce Mn^{2+} concentration in reaction (Figure 1b). The slower crystallization effect of EDTA has been confirmed in recent papers.^[21,41-43] The PDA@MnHCF sample was prepared by dispersing the MnHCF to the DA precursor solution. After 24 h of stirring, DA spontaneously polymerized on the surface of MnHCF and form a homogeneous coating layer, as shown in Figure 1c. Different from the polyhedral shape of MnHCF, the PDA@MnHCF exhibits spherical morphology, suggesting the successful coating of PDA. Figure 1d presents the XRD characterization of three samples. Among them, the characteristic peaks (002, 022, and 040 peaks) of MnHCF (without EDTA) were weaker, which confirmed its poorer crystallinity. With the chelation function of EDTA, the MnHCF and PDA@MnHCF samples showed stronger diffraction peaks indicating their better crystallinities. In addition, the diffraction peaks remain almost the same for both samples, suggesting that the PDA coating process without obvious influence on the crystallization of MnHCF. The patterns of the samples match well with the standard card JCPDS NO. 51-1896 ($KMn[Fe(CN)_6] \cdot 2H_2O$). Therefore, the chelation function of EDTA could also enhance the quality of MnHCF cathode with or without PDA coating. Further characterization of MnHCF cathodes were mainly between with or without PDA coating.

Figure 2 showed the electrochemical performance of AZIBs with the MnHCF and PDA@MnHCF cathodes. The charge/discharge curves of MnHCF were shown in Figure 2a. At the first cycle, there were two redox plateaus at about 1.8 and 1.6 V, corresponding to the redox reactions at Mn and Fe sites in MnHCF, respectively.^[44] At the 10th cycle, the 1.6 V plateau disappeared, which could be understood by the disintegration of MnHCF. PDA@MnHCF showed a similar trend in the first ten cycles except lower initial coulombic efficiency (ICE). The lower ICE is probably related to the CEI formation in PDA layer and results in improved cycle stability. Initial capacity loss could be explained by dissolution of Mn ions and substitution of MnHCF to ZnHCF. Such phenomenon was reported by recent EXAFS study.^[39] Interestingly, the capacity gradually increases after the initial decrease. The maximum capacity appears at about the 68th cycle. At the 100th cycle, the capacity still exceeded the 10th cycle (Figure 2b). The change of capacity was due to the appearance of a new plateau at about 1.3 V and slightly increased capacity at the higher voltage plateau. In both samples, this plateau appears, but with PDA coating, two plateaus showed higher capacity and appeared longer in cycles while the plateaus quickly disappeared in bare MnHCF sample. The new plateau could be explained by the formation of MnO_2 .^[40] Therefore, with PDA coating the dissolution of Mn ions could be restrained and some of Mn ions were formed MnO_2 intermediate phase, providing additional capacity after initial decrease. Without PDA coating, the MnO_2 was dissolved quickly in electrolyte and caused continuous capacity fading.

Figure 2c showed the cycling performance of the two samples at a low current density of $0.2 A g^{-1}$. The discharge specific capacity of PDA@MnHCF was $99.5 mAh g^{-1}$ at the first cycle while MnHCF exhibits a lower specific capacity of $98.5 mAh g^{-1}$. The MnHCF cathode without EDTA showed the lowest initial capacity.

During cycles, the bare MnHCF sample showed continuously reduced capacity and retained 65% before failed at the 190th cycle. The MnHCF cathode without EDTA showed the worst cycling performance and failed around 180 cycles with a capacity retention of 45%, as shown in (Figure S2, Supporting Information). Interestingly, PDA@MnHCF showed a gradual capacity rise from the 10th to 70th cycles, with a maximum discharge capacity even higher than the first cycle ($100.7 mAh g^{-1}$). The capacity retention at the 200th cycle reaches 69.7%, higher than the bare sample. The capacity rise was observed at other current densities as well. At the current density of $0.1 A g^{-1}$, the specific capacity of PDA@MnHCF increases from 93 to $114 mAh g^{-1}$ on the 5th cycle through the 30th cycle. In the meantime, the capacity of bare MnHCF exhibited monotonic decreased from 98.3 to $53.6 mAh g^{-1}$ until it failed at the 155th cycle (Figure S3, Supporting Information). Therefore, the capacity rise only occurred in the samples with PDA coating, which successfully improved the specific capacity of the MnHCF cathode.

In addition to its high reversible capacity and high voltage, the PDA@MnHCF also showed better rate performance (Figure 2d). The discharge specific capacities were 87.2 , 85.1 , 78.9 , 68.0 , 60.8 , and $54.5 mAh g^{-1}$ at current densities of 0.05 , 0.1 , 0.2 , 0.5 , 1.0 , and $2.0 A g^{-1}$. For MnHCF, those values were 87.6 , 85.8 , 73.9 , 61.3 , 55.2 , and $48.5 mAh g^{-1}$. It could be found that PDA@MnHCF provided higher capacity at current densities of $0.2 A g^{-1}$ and above. Subsequently, when the current was set back to $0.2 A g^{-1}$, the capacity of PDA@MnHCF recovered to $72.5 mAh g^{-1}$ with a retention rate of 91.9%, while those of MnHCF were $62.7 mAh g^{-1}$ and 84.8%. The improved rate performance could be explained by the hydrophilicity of PDA layer, which enhanced interfacial contact between cathode and aqueous electrolyte, resulting in faster Zn^{2+} ions diffusion and desolvation process.^[34,45] Figure 2e showed the long cycling performance for PDA@MnHCF cathode and MnHCF cathode batteries at a $2.0 A g^{-1}$. The increase trend in specific capacity of PDA@MnHCF still maintained in the 2000 cycle, with the highest discharge capacity of $45.6 mAh g^{-1}$. In contrast, the MnHCF cathode continuously decayed to $22.3 mAh g^{-1}$ after 2000 cycles. For the cycling data, it seemed that rise of capacity in PDA@MnHCF was largely irrelevant to charging and discharge current densities. Instead, it appeared to be solely relied on the total time of cycling.

To reveal the reason of the gradual increase in the specific capacity of PDA@MnHCF, SEM and XRD of the MnHCF and PDA@MnHCF cathodes were conducted to analyze the morphology and crystallographic structure at different cycles (0th, 5th, 10th, 20th, and 50th). Firstly, the SEM results of bare MnHCF cathodes were shown in Figure 3a,e. The larger polyhedral particles were MnHCF, and the smaller spherical particles were conductive black carbon. These SEM images showed significant morphology change of MnHCF during cycling process. Before cycling, the cathode sample kept a polyhedral morphology (Figure 3a). When the cycle number increased, the larger polyhedral particles disintegrated into smaller irregular particles. Compared to the 0th cycle, the polyhedral morphology was no longer clear at the 5th cycle (Figure 3b). At the 10 and 20th cycle (Figure 3c,d), the MnHCF particles became significantly smaller with flakes peeled off exposing interior of MnHCF particles. At the 50th cycle

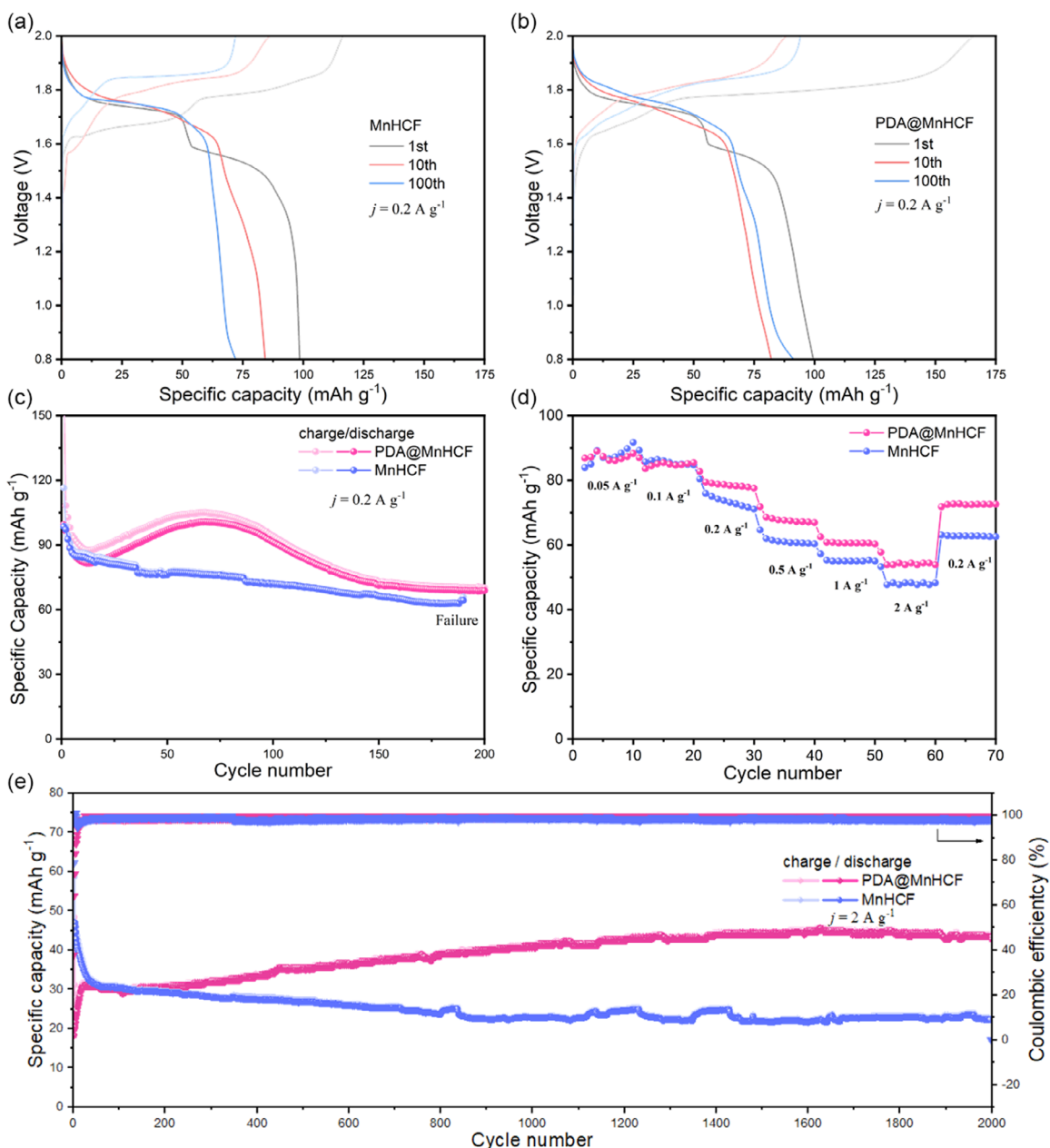


Figure 2. Electrochemical performances of PDA@MnHCF cathode batteries and MnHCF cathode batteries. The galvanostatic charge and discharge curves of a) MnHCF cathode batteries b) and PDA@MnHCF cathode batteries at 0.2 A g^{-1} at the 1st, 10th, and 100th cycles. c) Cycling stabilities of MnHCF cathode and PDA@MnHCF cathode batteries within 200 cycles at 0.2 A g^{-1} . d) Rate performances of MnHCF cathode and PDA@MnHCF cathode batteries. e) Long-term cyclabilities of the PDA@MnHCF cathode and MnHCF cathode batteries at a current density of 2.0 A g^{-1} .

(Figure 3e), it was difficult to distinguish the large MnHCF particles, the small conductive carbon black particles were mixed with the decomposed small particles, and the polyhedral structure of the MnHCF disappeared.

Combined with the analysis of the characteristic peaks in the XRD patterns in Figure 3f, the main compound in the MnHCF cathode before cycling was $\text{KMn}(\text{II})[\text{Fe}(\text{III})(\text{CN})_6] \cdot 2\text{H}_2\text{O}$ (potassium manganese iron cyanide hydrate, JCPDS NO.51-1896). However, at the 5th, 10th, 20th, and 50th cycles, the main compound in the MnHCF cathode turned into $\text{Zn}_2[\text{Fe}(\text{II})(\text{CN})_6]$ (zinc iron cyanide, JCPDS NO. 24-1441), and there were almost no peaks from

$\text{KMn}[\text{Fe}(\text{CN})_6]$. In addition, the intensity of the characteristic peaks of $\text{Zn}_2[\text{Fe}(\text{II})(\text{CN})_6]$ became stronger, indicating that the content of $\text{Zn}_2[\text{Fe}(\text{II})(\text{CN})_6]$ further increased with cycling. Therefore, the small particles formed on the surface after cycling in the SEM images should be ZnHCF particles, which demonstrates that severe manganese dissolution occurred in the MnHCF cathode during the charging and discharging process. At the same time, a large amount of Zn^{2+} ions in the electrolyte replaced the manganese sites to coordinate with ferrocyanide and formed ZnHCF. As a result, the change in shape in the SEM image originated from the collapse of the MnHCF structure and the formation of the

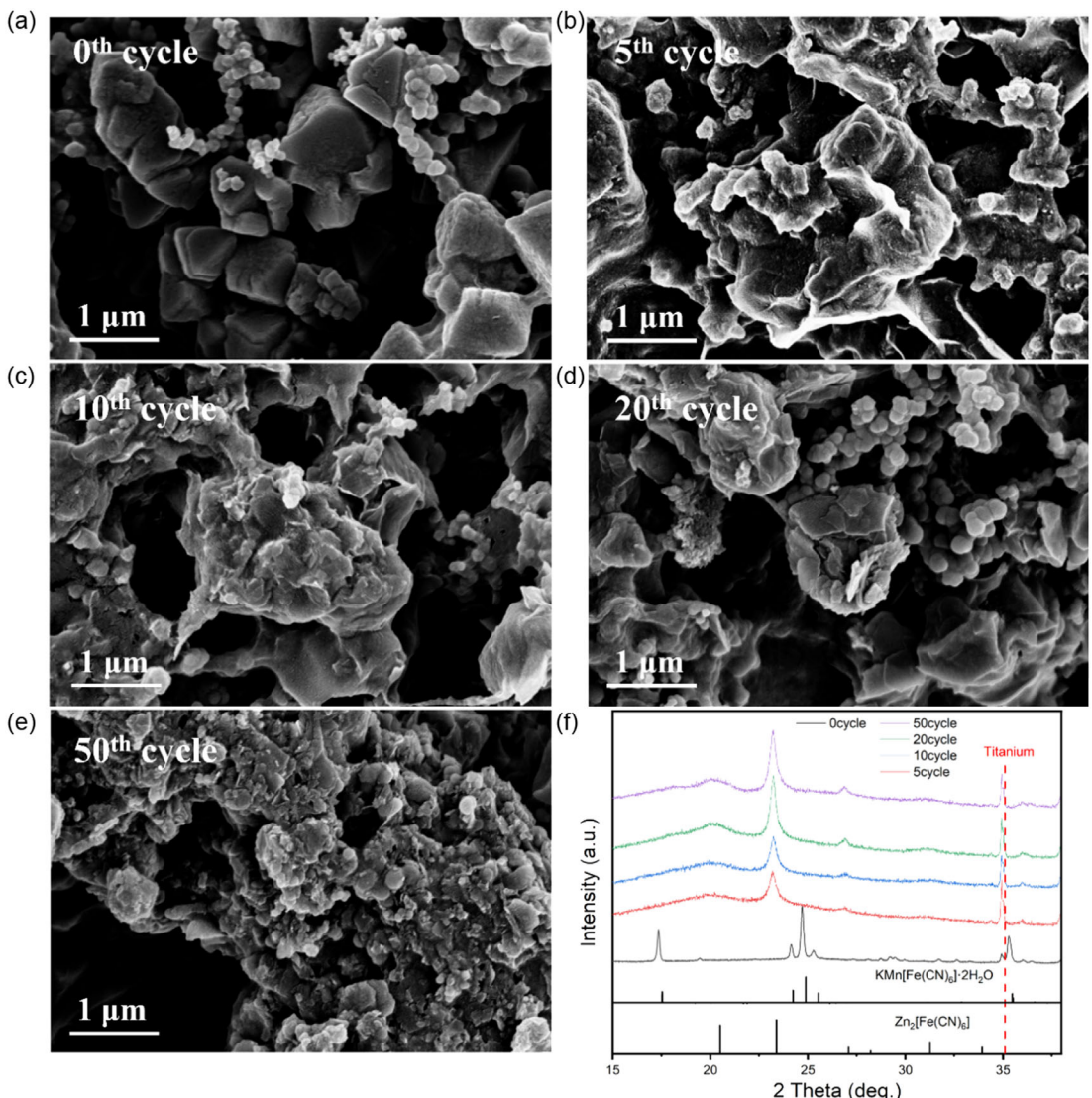


Figure 3. The SEM images of MnHCF cathode at the a) 0th cycle, b) 5th cycle, c) 10th cycle, d) 20th cycle, e) and 50th cycle. f) The XRD patterns of MnHCF cathode at the 0th cycle, 5th cycle, 10th cycle, 20th cycle, and 50th cycle.

ZnHCF. In addition, the Zn was electrochemically inert in ZnHCF and caused continuous capacity decay.

In contrast, the PDA@MnHCF cathode could maintain its original morphology better after cycles. At the 5th and 10th cycles (Figure 4b,c), the size of PDA@MnHCF particles remains nearly unchanged with gradual loss of its polyhedral shape. In the subsequent cycles (Figure 4d,e), the disintegration of the PDA@MnHCF particles were also slower, without any sign of flakes peeling off from the particles. The XRD results of PDA@MnHCF cathode are shown in Figure 4f. The characteristic peaks of KMn[Fe(CN)₆] could be detected in the spectra till the 20th cycle. The peak from ZnHCF appeared much later, only detected after 50 cycles. The evolution of XRD spectra confirmed that the disintegration of MnHCF was greatly retarded.

To qualitatively determine the electrochemical contribution of different compounds in cycles, incremental capacity (IC) analysis was derived from the charge and discharge curves, and the dQ/dV curves could provide detailed information on redox

plateaus.^[46,47] Different from conventional IC analysis, specific capacity (Q_m) eliminated the differences caused by different active materials. The area of the curve directly represented the specific capacity, which could provide data for analyzing capacity contribution of different redox reaction.^[46] The IC analysis of the batteries is based on the specific capacity data in Figure 2c. The analysis results of the batteries with PDA@MnHCF and MnHCF cathode were shown in Figure 5a,b, respectively. Among the peaks characterized by dQ_m/dV , the higher voltage peak originated from the Mn site in PBAs, while the low voltage peak represented the redox reaction peak of Fe.^[48,49] At the 1st cycle in Figure 5a, the curve showed two charge and discharge peaks from the Fe²⁺/Fe³⁺ and Mn²⁺/Mn³⁺ redox plateaus at 1.57/1.65 V and 1.73/1.80 V, respectively. At the 10th cycle, the Fe²⁺/Fe³⁺ redox reaction peaks shift to higher voltage. This was caused by enhanced lattice field when Mn substituted by Zn. After substitution, the lattice of ZnHCF becomes smaller, which increased the energy level splitting, giving larger potential of Fe at low spin

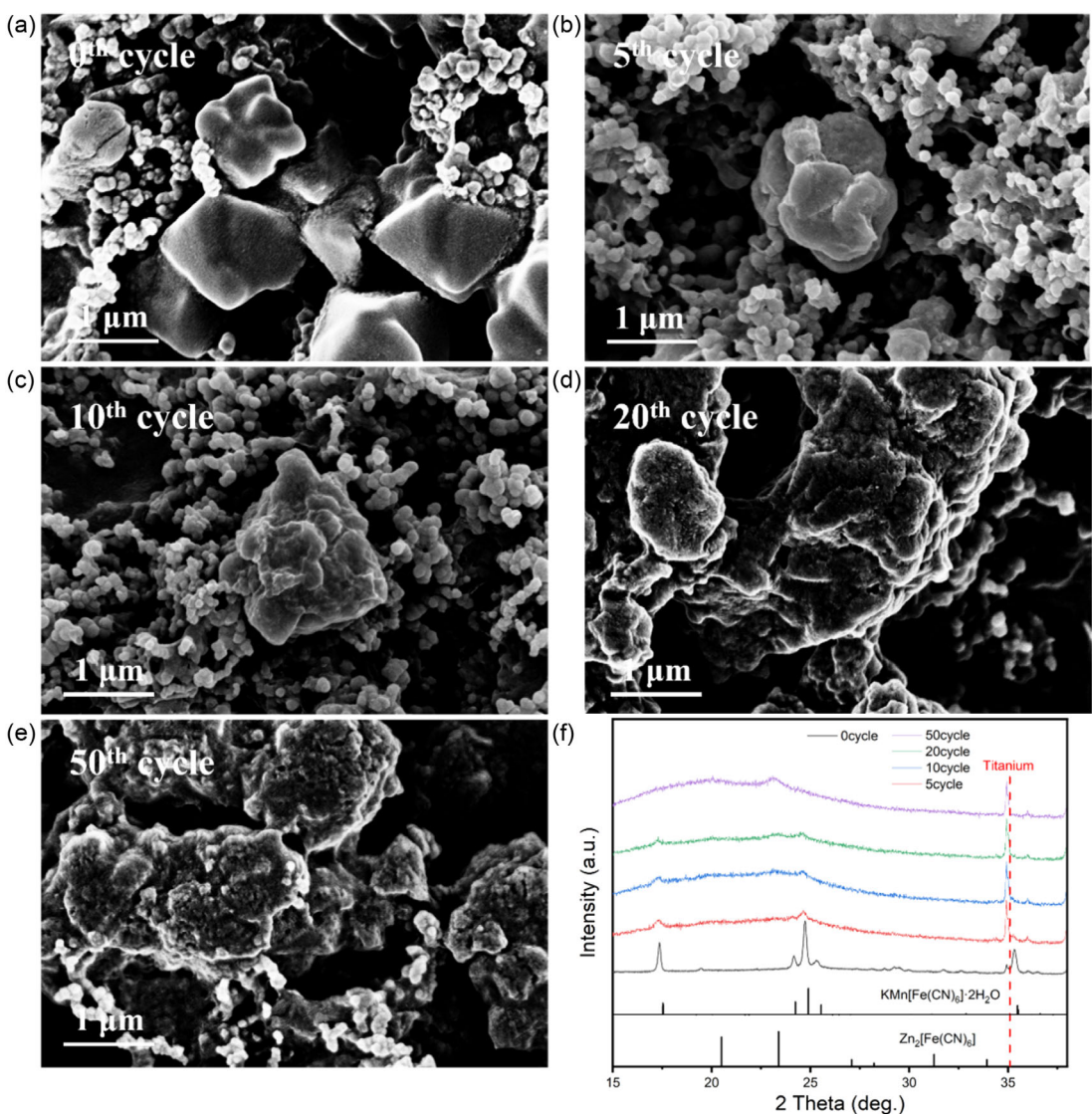


Figure 4. The SEM images of PDA@MnHCF cathode at the a) 0th cycle, b) 5th cycle, c) 10th cycle, d) 20th cycle, e) and 50th cycle. f) The XRD patterns of PDA@MnHCF cathode at the 0th cycle, 5th cycle, 10th cycle, 20th cycle, and 50th cycle.

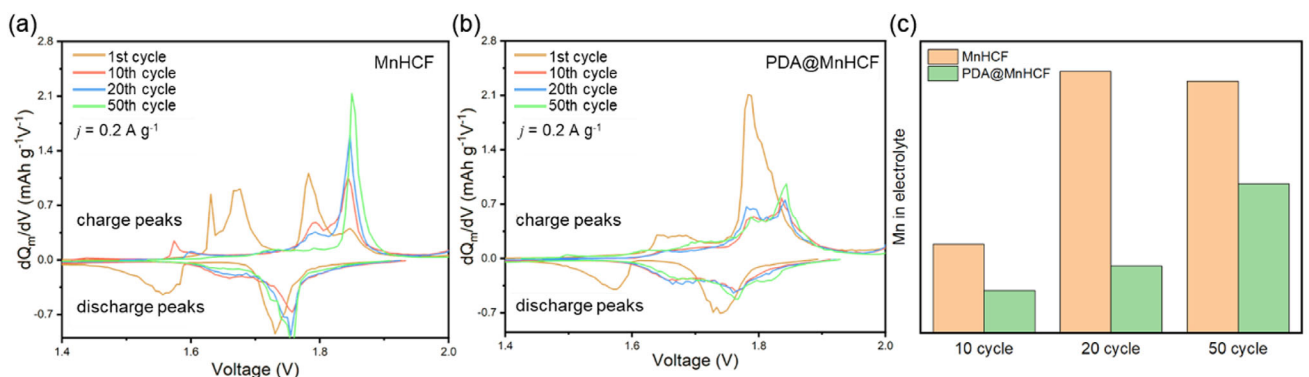


Figure 5. The IC analysis of a) PDA@MnHCF cathode battery and b) MnHCF cathode battery. c) The ICP-MS analysis to the electrolyte at the 10th, 20th, and 50th cycle.

state. The gradual increased $\text{Fe}^{2+}/\text{Fe}^{3+}$ voltage was also a sign of transition from MnHCF to ZnHCF. Finally, the Fe and Mn redox peaks appeared overlapped when significant transition of

MnHCF to ZnHCF happens.^[17,50] For the dQ_m/dV curves, PDA@MnHCF almost unchanged from the 10th to the 50th cycle (Figure 5b), indicating lesser transition from MnHCF to ZnHCF.

Figure 5c depicted the concentrations of manganese in electrolyte after 10, 20 and 50 cycles by inductively coupled plasma mass spectrometry (ICP-MS) measurement. For bare MnHCF cathode, the concentration quickly saturated after 20 cycles, indicating that surface manganese is quickly depleted. In contrast, the concentration increased much slower in the electrolyte with PDA@MnHCF cathode. The concentration is about 60% of that in bare MnHCF electrolyte after 50 cycles, indicating a much slower manganese dissolution process. These results confirmed that the PDA coating could suppress manganese dissolution effectively, and maintained electrochemical performance of MnHCF, which agreed with the observations in SEM and XRD (Figure S3, Supporting Information).

To quantitatively study the contributions of different redox reactions to the capacity during cycles, the selected dQ_m/dV curves in first 150 cycles were shown in Figure 6a. The 1st curve showed two peaks at 1.74 and 1.57 V originated from Mn and Fe in MnHCF, respectively. In total, the discharge capacity reached 99.5 mAh g⁻¹. After the first 10 cycles' activation, these two peaks shifted to 1.76 and 1.67 V.^[50–53] The intensity of both peaks remained nearly unchanged, suggesting its good cycle stability. Meanwhile, the peak positions only reduced slightly to about 0.01 V. After 20 cycles, the third peak at 1.80 V gradually appears,

which should be from Fe in ZnHCF.^[49] The formation of ZnHCF was the consequence of Zn substitution of Mn in MnHCF. The XRD signal of ZnHCF was observed in both cathodes clearly after 50 cycles. The representative fittings at the 10th, 80th, and 140th cycle of discharge curves were shown in Figure 6b,d. The fitting of the first cycle was shown in (Figure S4, Supporting Information). From the fitting results, the Fe in ZnHCF gradually increased and occupied about 32.3% of total capacity. The temporary increase of total capacity in Figure 2c could be attributed to the presence of the fourth peak at 1.35 V, which contributed 10.4% of total capacity to the 80th cycle. The origin of this peak probably due to the formation of MnO₂ after the encapsulation of PDA layer.^[54] The encapsulation reduced the direct contact of MnHCF with electrolyte, retards Mn dissolution and caused accumulation of Mn ions in the form of oxides. This intermediate MnO₂ phase provides additional capacity within the first 120 cycles. After that, the contribution of this intermediate phase gradually ceased, suggesting its final disintegration. The fittings of other cycles were shown in (Figure S5, Supporting Information). On the contrary, the cathode without PDA coating presented lesser contribution from 1.80 V, though the signal of ZnHCF in XRD was still stronger (Figure S6 and S7, Supporting Information). This observation suggested that without PDA

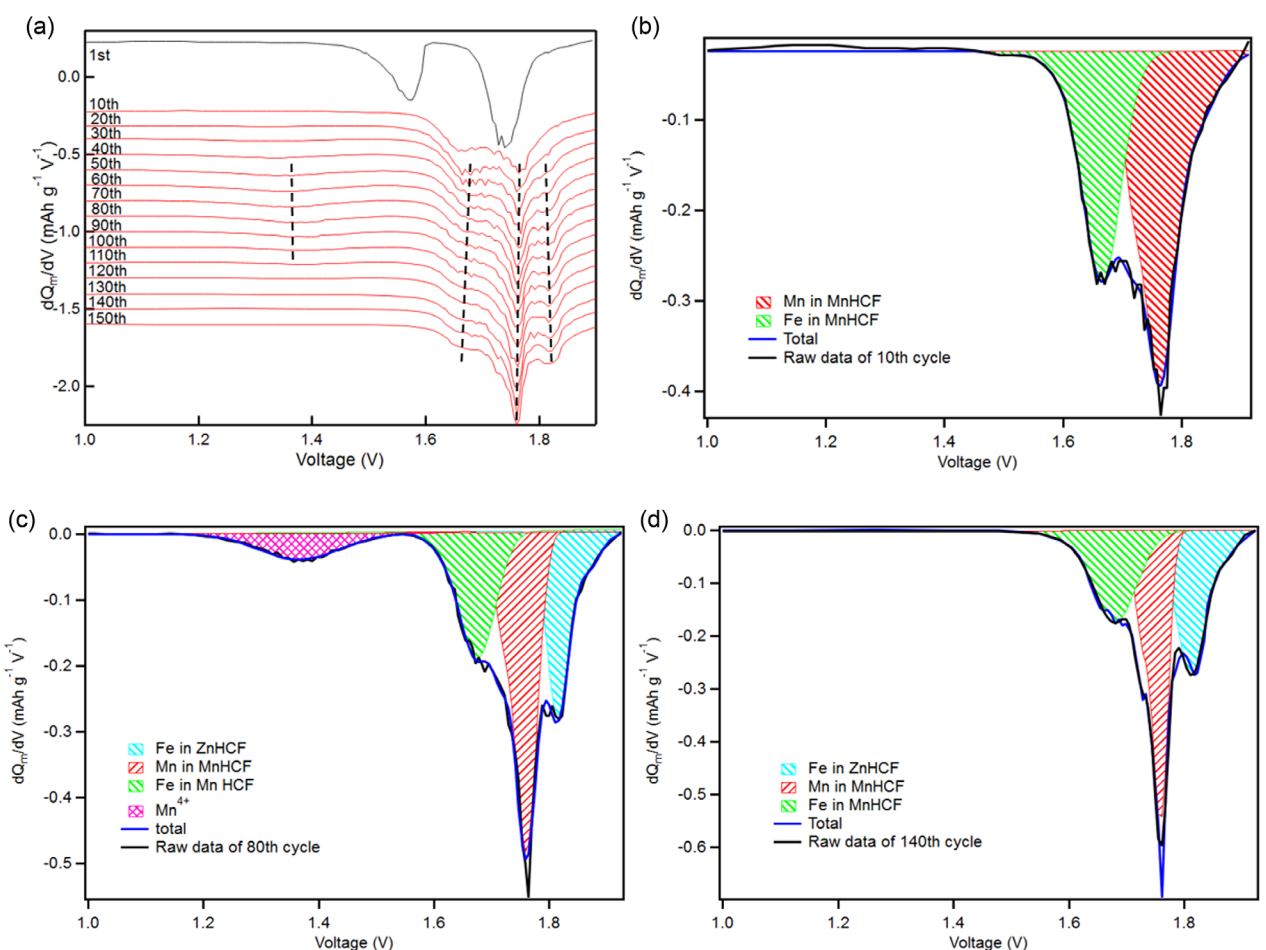


Figure 6. The evolution of dQ/dV curves of PDA@MnHCF cathode in full cell. a) dQ/dV curves of every ten cycles, b) fitting of the 10th cycle, c) fitting of the 80th cycle, and d) fitting of the 140th cycle.

coating, the formed ZnHCF was largely electrochemically inactive. Furthermore, no signal of the fourth peak was seen within 150 cycles, suggesting that the intermediate phase could not form. For dQ_m/dV analysis, it could be concluded that the PDA coating slows down the dissolution of Mn ions, stabilizes capacity from ZnHCF, and even temporarily contributes more capacity from the formation of MnO_2 intermediate phase.

3. Conclusion

In summary, a PDA-coated MnHCF material (PDA@MnHCF) was prepared to suppress manganese dissolution. Without PDA layer, the bare MnHCF severely changed to ZnHCF in less than 10 cycles, while the PDA@MnHCF sample showed obvious ZnHCF signal in XRD after 50 cycles and stabilized after 140 cycles in quantitative dQ/dV analysis. The slowed dissolution process also induced a capacity rise within the first 100 cycles due to additional contribution from $\text{Fe}^{2+}/\text{Fe}^{3+}$ in MnHCF and ZnHCF as well as generated intermediate MnO_2 . As a result, the full cell exhibited a gradual increase trend within 200 cycles with a high capacity of 100.7 mAh g^{-1} at low current density of 0.2 A g^{-1} . At a high current density of 2.0 A g^{-1} , the PDA@MnHCF battery still exhibited a 45.5 mAh g^{-1} capacity after 2000 cycles. Our results demonstrated the beneficial effect of PDA in suppressing Mn dissolution for MnHCF cathode and quantitatively revealed the evolution of different compounds in PDA@MnHCF cathode during cycling.

4. Experimental Section

Materials Synthesis: Synthesis of manganese hexacyanoferrate (MnHCF and MnHCF no EDTA)

The manganese(II) hexacyanoferrate (MnHCF) was synthesized by coprecipitation method. First, 73.5 mg of manganese(II) acetate tetrahydrate ($\text{MnAc}_2 \cdot 4\text{H}_2\text{O}$, 0.3 mmol), 70.1 mg of EDTA dipotassium salt dihydrate ($\text{K}_2\text{EDTA} \cdot 2\text{H}_2\text{O}$, 0.2 mmol), and 400 mg of polyvinylpyrrolidone (PVP, M.W. 58,000, $K = 30$) were dissolved in 20.0 mL deionized water as solution A. Second, 105.4 mg of potassium hexacyanoferrate(III) ($\text{K}_3[\text{Fe}(\text{CN})_6]$, 0.32 mmol) was dissolved in 20.0 mL of deionized water as solution B. Then, solution B was dropped into solution A with constant stirring. After the obtained brown mixed solution, it was aged at room temperature (25°C) for 24 h under atmospheric pressure. Finally, the precipitate was centrifuged by centrifuge and washed three times each with deionized water and ethanol, and it was dried in vacuum oven at 80°C for 12 h to obtain MnHCF. For the synthesis of MnHCF no EDTA sample, EDTA was not added.

Synthesis of PDA coated manganese hexacyanoferrate (PDA@MnHCF)

Firstly, 48.48 mg of trishydroxymethylaminomethane (Tris) was added into 40 mL of deionized water, and 120 mg of MnHCF was then added; the above solution was ultrasonically treated for 10 min. Then, 40 mg of DA hydrochloride (3-hydroxytyramine hydrochloride) was added to the above suspension and stirred at room temperature for 24 h until a homogeneous mixture formed.^[36,37] Finally, the precipitation was washed three times with deionized water and ethanol respectively and then dried in vacuum oven at 80°C for 12 h to obtain PDA@MnHCF.

Characterizations

The crystalline phase identification of the samples was performed by using X-ray diffraction (XRD, Cu K α , $\lambda = 0.154 \text{ nm}$). The morphologies of sample were collected by scanning electron microscopy (SEM, Sigma, Carl Zeiss). The concentration of manganese ions in the electrolyte was measured by ICP-MS.

Electrochemical Measurements

The cathode slurry was prepared with MnHCF/PDA@MnHCF, Super P conductive carbon black, and polyvinylidene fluoride binder (with a weight ratio of 7:2:1 in *N*-methyl pyrrolidone (NMP) solvent) and cast on titanium foil (20 μm in thickness, 12 mm in diameter). Then, the electrodes were dried in a vacuum oven at 80°C for 2 h and the mass loading is about $0.9\text{--}1.4 \text{ mg cm}^{-2}$. CR2025 cells were assembled with MnHCF/PDA@MnHCF cathode and zinc anode (100 μm in thickness, 16 mm in diameter) and 4 M zinc trifluoromethanesulfonate ($\text{Zn}(\text{OTF})_2$) in H_2O as electrolyte. Galvanostatic tests of cells between 0.8 and 2.0 V are conducted with a battery test system (Neware CT-4008).

Preparation for ICP-MS Measurement

Fifteen batteries with PDA@MnHCF cathode were prepared and divided into 5 groups. Each group contained 3 cells and underwent galvanostatic charge and discharge process and terminated at the 0th (no cycle), 5th, 10th, 20th, and 50th cycles. Then, the cells were disassembled, and the glass fiber separator were taken out and soaked in 5 mL of deionized water and left for 24 h. Lastly, the supernatant was used for ICP-MS measurement.

Acknowledgements

H.O. and H.Z. contributed equally to this work. This work was supported by the Macau Science and Technology Development Fund for funding (File No. 0013/2021/AMJ, and 0082/2022/A2) and Multi-Year research grant (MYRG2020-00283-IAPME, MYRG2022-00266-IAPME, and MYRG-GRG2023-00224-IAPME-UMDF) from the Research & Development Office at University of Macau.

Conflict of Interest

The authors declare no conflict of interest.

Data Availability Statement

The data that support the findings of this study are available from the corresponding author upon reasonable request.

Keywords: manganese dissolution • mechanism analyses • polydopamine • Prussian blue • zinc ion batteries

- [1] S. Zhang, J. Chen, W. Chen, Y. Su, Q. Gou, R. Yuan, Z. Wang, K. Wang, W. Zhang, X. Hu, Z. Zhang, P. Wang, F. Wan, J. Liu, B. Li, Y. Wang, G. Zheng, M. Li, J. Sun, *Angew. Chem. Int. Ed.* **2025**, *64*, e202424184.
- [2] X. Zhang, X. Ma, H. Bi, Y. Zhang, P. Mi, F. Liu, X. Jin, Y. Chen, K. Zhang, J. Wang, Y. Dong, *Adv. Funct. Mater.* **2025**, *35*, 2411990.

- [3] H. Luo, Q. Gou, Y. Zheng, K. Wang, R. Yuan, S. Zhang, W. Fang, Z. Luogu, Y. Hu, H. Mei, B. Song, K. Sun, J. Wang, M. Li, *ACS Nano* **2025**, *19*, 2427.
- [4] Q. Gou, S. Zhang, H. Mei, C. Liu, H. Luo, K. Wang, Y. Hu, B. Song, Y. Zheng, M. Qiao, M. Li, *J. Mater. Chem. A* **2025**, *13*, 7766.
- [5] Q. Gou, H. Luo, L. Qu, F. Yu, K. Wang, S. Zhang, Z. Luogu, B. Zhang, Y. Zheng, B. Song, J. Wang, M. Li, *J. Energy Chem.* **2025**, *101*, 191.
- [6] H. Ouyang, S. Min, J. Yi, X. Liu, F. Ning, J. Qin, Y. Jiang, B. Zhao, J. Zhang, *Green Energy Environ.* **2023**, *8*, 1195.
- [7] K. Wang, H. Li, Z. Xu, Y. Liu, M. Ge, H. Wang, H. Zhang, Y. Lu, J. Liu, Y. Zhang, Y. Tang, S. Chen, *Adv. Energy Mater.* **2024**, *14*, 2304110.
- [8] J. Deng, G. Xue, C. Li, S. Zhao, Y. Zheng, Y. He, R. Yuan, K. Wang, T. Mo, Y. Xiang, Y. Chen, Y. Geng, L. Wang, G. Feng, X. Hou, M. Li, *J. Am. Chem. Soc.* **2025**, *147*, 5943.
- [9] J. Huang, J. Zeng, K. Zhu, R. Zhang, J. Liu, *Nano-Micro Lett.* **2020**, *12*, 110.
- [10] S. Zhang, Q. Gou, W. Chen, H. Luo, R. Yuan, K. Wang, K. Hu, Z. Wang, C. Wang, R. Liu, Z. Zhang, Y. Lei, Y. Zheng, L. Wang, F. Wan, B. Li, M. Li, *Adv. Sci.* **2024**, *11*, 2404968.
- [11] X. Zhang, M. Xia, T. Liu, N. Peng, H. Yu, R. Zheng, L. Zhang, M. Shui, J. Shu, *Chem. Eng. J.* **2021**, *421*, 127767.
- [12] M. Huang, J. Meng, Z. Huang, X. Wang, L. Mai, *J. Mater. Chem. A* **2020**, *8*, 6631.
- [13] G. Zampardi, F. La Mantia, *Curr. Opin. Electrochem.* **2020**, *21*, 84.
- [14] M. Jiang, Z. Hou, L. Ren, Y. Zhang, J.-G. Wang, *Energy Storage Mater.* **2022**, *50*, 618.
- [15] L. Ma, S. Chen, C. Long, X. Li, Y. Zhao, Z. Liu, Z. Huang, B. Dong, J. A. Zapien, C. Zhi, *Adv. Energy Mater.* **2019**, *9*, 1902446.
- [16] M. Li, M. Maisuradze, R. Sciacca, I. Hasa, M. Giorgetti, *Batteries Supercaps* **2023**, *6*, e202300340.
- [17] L. Ma, H. Cui, S. Chen, X. Li, B. Dong, C. Zhi, *Nano Energy* **2021**, *81*, 105632.
- [18] D. Zuo, C. Wang, J. Han, Q. Han, Y. Hu, J. Wu, H. Qiu, Q. Zhang, X. Liu, *J. Mater. Sci. Technol.* **2022**, *114*, 180.
- [19] X. Zhu, F. Meng, Q. Zhang, L. Xue, H. Zhu, S. Lan, Q. Liu, J. Zhao, Y. Zhuang, Q. Guo, B. Liu, L. Gu, X. Lu, Y. Ren, H. Xia, *Nat. Sustainability* **2021**, *4*, 392.
- [20] F. Gebert, D. L. Cortie, J. C. Bouwer, W. Wang, Z. Yan, S.-X. Dou, S.-L. Chou, *Angew. Chem., Int. Ed.* **2021**, *60*, 18519.
- [21] X. Li, Y. Shang, D. Yan, L. Guo, S. Huang, H. Y. Yang, *ACS Nano* **2022**, *16*, 453.
- [22] B. Luo, H. Wang, C. Chen, L. Liu, K. Wu, H. Li, D. Ye, Y. Li, L. Cui, J. Qiao, *J. Colloid Interface Sci.* **2024**, *675*, 639.
- [23] H. Gao, S. Xin, L. Xue, J. B. Goodenough, *Chem* **2018**, *4*, 833.
- [24] K. Hurlbutt, S. Wheeler, I. Capone, M. Pasta, *Joule* **2018**, *2*, 1950.
- [25] M. Pasta, R. Y. Wang, R. Ruffo, R. Qiao, H.-W. Lee, B. Shyam, M. Guo, Y. Wang, L. A. Wray, W. Yang, M. F. Toney, Y. Cui, *J. Mater. Chem. A* **2016**, *4*, 4211.
- [26] X. Wang, B. Wang, Y. Tang, B. B. Xu, C. Liang, M. Yan, Y. Jiang, *J. Mater. Chem. A* **2020**, *8*, 3222.
- [27] G. Ni, B. Han, Q. Li, Z. Ji, B. Huang, C. Zhou, *ChemElectroChem* **2016**, *3*, 798.
- [28] H. Wang, W. Wei, X. Liu, S. Xu, Y. Dong, R. He, *Energy Storage Mater.* **2023**, *55*, 597.
- [29] W. Deng, Z. Li, Y. Ye, Z. Zhou, Y. Li, M. Zhang, X. Yuan, J. Hu, W. Zhao, Z. Huang, C. Li, H. Chen, J. Zheng, R. Li, *Adv. Energy Mater.* **2021**, *11*, 2003639.
- [30] Y. Li, L. Wu, C. Dong, X. Wang, Y. Dong, R. He, Z. Wu, *Energy Environ. Mater.* **2023**, *6*, e12423.
- [31] Y. Liu, D. He, Y. Cheng, L. Li, Z. Lu, R. Liang, Y. Fan, Y. Qiao, S. J. S. Chou, *Nano Micro Small* **2020**, *16*, 1906946.
- [32] Q. Han, Y. Li, L. Han, Z. Lu, L. Liu, *Synth. Met.* **2024**, *301*, 117510.
- [33] Y. Xue, H. Zhou, Z. Ji, X. Shen, J. Cao, J. Pu, L. Kong, A. Yuan, *Appl. Surf. Sci.* **2023**, *633*, 157580.
- [34] T. Wang, P. Wang, L. Pan, Z. He, L. Dai, L. Wang, S. Liu, S. C. Jun, B. Lu, S. J. A. E. M. Liang, *Adv. Energy Mater.* **2023**, *13*, 2203523.
- [35] Q. Gou, H. Luo, Y. Zheng, Q. Zhang, C. Li, J. Wang, O. Odunmbaku, J. Zheng, J. Xue, K. Sun, M. Li, *Small* **2022**, *18*, 2201732.
- [36] Y. Liu, D. He, Y. Cheng, L. Li, Z. Lu, R. Liang, Y. Fan, Y. Qiao, S. Chou, *Nano Micro Small* **2020**, *16*, 1906946.
- [37] B. Wang, Y. Zeng, P. Chen, J. Hu, P. Gao, J. Xu, K. Guo, J. Liu, *ACS Appl. Mater. Interfaces* **2022**, *14*, 36079.
- [38] G. Zhang, J. Zhu, L. Lin, Y. Liu, S. Li, Q. Li, X.-X. Liu, X. J. C. S. Sun, *Chem. Sci.* **2024**, *15*, 3545.
- [39] Y. K. Jeong, S. H. Park, J. W. Choi, *ACS Appl. Mater. Interfaces* **2018**, *10*, 7562.
- [40] H. Ouyang, S. Min, J. Yi, X. Liu, F. Ning, Y. Xu, Y. Jiang, B. Zhao, J. Zhang, *ACS Appl. Mater. Interfaces* **2022**, *14*, 53648.
- [41] K. Wang, Z. Xu, H. Li, H. Wang, M. Ge, J. Liu, S. Li, Z. Hu, M. Zhu, Y. Zhang, Y. Tang, S. Chen, *J. Mater. Sci. Technol.* **2023**, *164*, 102.
- [42] L. Shen, Y. Jiang, Y. Jiang, J. Ma, K. Yang, H. Ma, Q. Liu, N. Zhu, *ACS Appl. Mater. Interfaces* **2022**, *14*, 24332.
- [43] L. Deng, J. Qu, X. Niu, J. Liu, J. Zhang, Y. Hong, M. Feng, J. Wang, M. Hu, L. Zeng, Q. Zhang, L. Guo, Y. Zhu, *Nat. Commun.* **2021**, *12*, 2167.
- [44] M. Du, P. Geng, C. Pei, X. Jiang, Y. Shan, W. Hu, L. Ni, H. Pang, *Angew. Chem., Int. Ed.* **2022**, *61*, e202209350.
- [45] L. Wang, H. Dang, T. He, R. Liu, R. Wang, F. J. B. E. Ran, *Battery Energy* **2024**, *3*, 20240001.
- [46] L. Zheng, J. Zhu, D. D.-C. Lu, G. Wang, T. He, *Energy* **2018**, *150*, 759.
- [47] D. Anseán, V. M. García, M. González, C. Blanco-Viejo, J. C. Viera, Y. F. Pulido, L. Sánchez, *IEEE Trans. Ind. Appl.* **2019**, *55*, 2992.
- [48] W. Chen, J. Wu, K. Fu, Z. Deng, X. Chen, H. Cai, X. Wu, B. Xing, W. Luo, L. Mai, *Small Methods* **2024**, *8*, 2300617.
- [49] M. Li, R. Sciacca, M. Maisuradze, G. Aquilanti, J. Plaisier, M. Berrettoni, M. Giorgetti, *Electrochim. Acta* **2021**, *400*, 139414.
- [50] J. Wu, J. Song, K. Dai, Z. Zhuo, L. A. Wray, G. Liu, Z. Shen, R. Zeng, Y. Lu, W. Yang, *J. Am. Chem. Soc.* **2017**, *139*, 18358.
- [51] C. Gao, Y. Lei, Y. Wei, H. Wang, F. Yuan, F. Kang, D. Zhai, *Chem. Eng. J.* **2022**, *431*, 133926.
- [52] Z. Li, T. Liu, R. Meng, L. Gao, Y. Zou, P. Peng, Y. Shao, X. Liang, *Energy Environ. Mater.* **2021**, *4*, 111.
- [53] Y. Gao, H. Yang, X. Wang, Y. Bai, N. Zhu, S. Guo, L. Suo, H. Li, H. Xu, C. Wu, *ChemSusChem* **2020**, *13*, 732.
- [54] H. Pan, Y. Shao, P. Yan, Y. Cheng, K. S. Han, Z. Nie, C. Wang, J. Yang, X. Li, P. Bhattacharya, K. T. Mueller, J. Liu, *Nat. Energy* **2016**, *1*, 16039.

Manuscript received: March 31, 2025

Revised manuscript received: May 9, 2025

Version of record online: